RSC Advances

PAPER

View Article Online
View Journal | View Issue

Cite this: *RSC Adv.*, 2026, **16**, 24055

First-principles study on strain-engineered photocatalytic performance in ferroelectric $K(Ta_{0.5}Nb_{0.5})O_3$

Xue Wen,[a] Rui Xia,[a] Yi-Min Zheng,[a] Qiao-Yue Chen,[a] Can Zhao,[a] Xin-Yuan Zhou,[a] Hong-Mei Yin,[ab] Li-Li Zhang *[a] and Yi-Neng Huang*[ac]

Based on first-principles calculations, this study systematically investigated the evolution of structural stability, electronic structure, and bulk photoelectric properties of $K(Ta_{0.5}Nb_{0.5})O_3$ (KTN) under biaxial strain ranging from −30% to 30%. The calculation results show that KTN maintains structural integrity throughout the strain range. Tensile strain (5–30%) enhances structural stability, with the system's binding energy decreasing from −7.3 eV to −7.9 eV, accompanied by a phase transition from tetragonal to monoclinic. Under −30% compressive strain, KTN stabilizes in the monoclinic phase. The projected crystal orbital occupation numbers indicate that the overall covalent bond strength of the system increases with the increase of strain, and the electron distribution of the O–Nb bond shows a non-monotonic change, reaching a peak of 0.085 at approximately −10% strain. Strain regulation significantly enhances ferroelectric polarization intensity and promotes the separation of photogenerated electron–hole pairs. Compressive strain continuously reduces the band gap, with the calculated minimum value being 0.838 eV at −30% strain (this value may be underestimated due to the limitations of the PBE functional). The carriers exhibit a "heavy hole-light electron" characteristic ($m_h^*/m_e^* \approx 2.4$), which is conducive to hole migration to the surface. Compressive strain (−30% to −15%) and 5% tensile strain can induce a redshift of the absorption edge, expanding the visible light response range. Notably, monoclinic KTN under −30% compressive strain shows an optimized trend in polarization intensity, carrier mobility, and light absorption rate. Although achieving ±30% strain through standard epitaxial growth techniques is currently difficult (this technique is usually limited to ±4% or so), exploring such extreme conditions enables us to separate the correlation between electronic effects and lattice instability and clearly reveal the regularity of orbital activity. This study provides theoretical guidance for strain engineering in the design of KTN-based photocatalytic materials, but to accurately predict actual photocatalytic activity (such as hydrogen evolution efficiency), systematic research combining surface reaction energy barriers, carrier recombination kinetics, and interface band bending effects is still needed.

Received 29th November 2025
Accepted 12th April 2026

DOI: 10.1039/d5ra09223j

rsc.li/rsc-advances

1 Introduction

Photocatalytic water splitting for hydrogen production is a key technology for the efficient conversion of solar energy into chemical energy in the form of hydrogen. However, its practical application is hindered by two major bottlenecks: the high recombination rate of photogenerated charge carriers and slow surface reaction kinetics.[1] Ferroelectric materials offer a promising solution to these challenges due to their built-in electric field, which arises from spontaneous polarization. This intrinsic field enables synergistic regulation of spatial charge separation and surface catalytic activity, thereby providing a unique physical mechanism for enhancing photocatalytic performance.[2] The spontaneous polarization in ferroelectric materials stems from the spatial displacement of positive and negative charge centers within the crystal lattice. The resulting internal electric field effectively prolongs the lifetime of separated photogenerated electron–hole pairs,[3] leading to a significant improvement in photocatalytic quantum efficiency.[4,5] A representative example is the ferroelectric material $BiOIO_3$,[6] in which the asymmetric arrangement of IO^{3-} groups gives rise to a strong intrinsic polarization field. This structure reduces the recombination rate of photogenerated carriers by 72% compared to conventional MoS_2 catalysts and increases the kinetic constant for pollutant degradation by *a* factor of 3.46,

[a]*College of Physics and Technology, Yili Normal University, Xinjiang Condensed Matter Phase Transitions and Microstructures Laboratory, Yining 835000, China. E-mail: zhanglili@ylnu.edu.cn; ynhuang@nju.edu.cn*

[b]*College of Physical Science and Technology, Xinjiang University, Urumqi, 830046, China*

[c]*National Laboratory of Solid State Microstructures, School of Physics, Nanjing University, Nanjing 210093, China*

unequivocally demonstrating the enhanced photocatalytic activity enabled by ferroelectric polarization.

Among numerous ferroelectric materials, KTN, a typical representative of the $KNbO_3$–$KTaO_3$ solid solution system, has emerged as a promising material in visible-light photo catalysis. This prominence stems from its broad spectral absorption (covering ultraviolet to visible regions), high carrier mobility (approximately 10^2 cm^2 V^{-1} s^{-1}), and tunable dielectric response, with a Curie temperature adjustable between 200 K and 500 K.[7] However, current research remains largely focused on the fundamental optoelectronic characterization of KTN, while a quantitative structure–activity relationship between its polarization intensity and photocatalytic performance is still lacking.[8,9] Specifically, the following critical aspects have yet to be elucidated: (1) the quantitative correlation between polarization-induced internal electric field strength and charge carrier separation efficiency; (2) the dynamic coupling mechanism between lattice distortion under strain regulation and the redox potential of surface catalytic sites; (3) the synergistic evolution of the electronic band structure (*e.g.*, bandgap width and band edge positions) and its effect on the expansion of the light absorption range. These unresolved issues represent major bottlenecks limiting the optimization of the photocatalytic performance of KTN.

In recent years, strain engineering has emerged as a promising strategy for modulating the electronic structure of functional materials, offering a novel avenue to overcome the limitations mentioned above. Both theoretical and experimental investigations have demonstrated that precise application of biaxial strain (ranging from −30% to 30%) enables effective control over lattice distortions in ferroelectric materials, thereby reconfiguring[10] the cooperative distribution of their intrinsic polarization and piezoelectric fields. For instance, under compressive strain, the bandgap of two-dimensional ferroelectric In_2Se_3 (ref. 11) can be tuned into the visible-light response range (0.5–1.5 eV), while its built-in electric field intensity is enhanced to 2.02 V nm^{-1}, resulting in a solar-to-hydrogen conversion efficiency of 6.6%. Similarly, strain engineering enables *R*3*c*-$CuNbO_3$ (ref. 12) to achieve simultaneous bandgap narrowing (to 1.5 eV) and improved photoconversion efficiency (up to 29.9%), highlighting its potential for application in ferroelectric photocatalytic materials. Nevertheless, current studies remain predominantly focused on performance optimization under single strain conditions. There is still a lack of systematic research on the multi-scale dynamic coupling mechanisms among structural stability, electronic properties, and photocatalytic performance across a broad strain range (−30% to 30%). Although this extreme range far exceeds the typical mismatch window of epitaxial films (usually around ±4%), it serves as a crucial theoretical limit to provide fundamental guidance for practical material design. Furthermore, exploring such large strains is physically justified by several realistic scenarios: (1) free-standing complex oxide membranes (*e.g.*, $SrTiO_3$) transferred to flexible or piezoelectric substrates can endure giant mechanical strains that surpass traditional epitaxial limits;[13] (2) nanostructures (*e.g.*, nanowires, nanoparticles) can sustain massive elastic strains compared to bulk materials due to their high surface-to-volume ratios and reduced defect densities;[14] (3) local chemical environments during catalysis (*e.g.*, ion intercalation or high-density oxygen vacancies) can induce extreme localized lattice distortions, making 30% a valid theoretical upper bound to capture these variations;[15] and (4) large compressive strains effectively emulate high-pressure physics experiments (*e.g.*, using diamond anvil cells), where lattice parameters decrease significantly under gigapascal pressures.[16] In particular, the strain-induced phase transition behavior (*e.g.*, tetragonal to monoclinic transformation) in solid-solution systems such as KTN and its impact on photocatalytic activity remain poorly understood.[17]

Building upon this foundation, the present study employs KTN as a model system and utilizes first-principles calculations to systematically investigate the evolution of structural stability, electronic properties, and photocatalytic performance under biaxial strain ranging from −30% to 30%. The specific objectives include: (1) elucidating the correlation between strain-induced lattice distortions (*e.g.*, redistribution of Mulliken charges) and phase transitions (tetragonal-to-monoclinic); (2) quantitatively analyzing the nonlinear strain-dependent modulation of ferroelectric polarization strength, anisotropy in carrier effective mass, and band edge shifts; and (3) establishing a quantitative structure–activity relationship encompassing polarization intensity, carrier migration efficiency, and light absorption range. The findings are expected to provide theoretical guidance for the strain engineering of KTN-based photocatalytic materials, while also offering a universal research framework for optimizing the performance of other ferroelectric solid-solution systems.[18] However, the strain range studied far exceeds the typical mismatch window of epitaxial films, aiming to explore the theoretical limits and mechanisms, and to provide fundamental guidance for material design within more practical strain ranges (such as ±5%).

2 Computational details

In this study, a 2 × 2 × 2 KTN supercell with the space group *P*4*mm* (No. 99) was constructed, having lattice parameters of $a = b = 8.0248$ Å, $c = 8.2093$ Å, and $\alpha = \beta = \gamma = 90°$. A schematic of the supercell is presented in Fig. 1, where panel (a) illustrates the ball-and-stick model and panel (b) shows the polyhedral representation. Regarding the B-site cations, the Ta and Nb atoms were arranged in a rock-salt (G-type) alternating configuration. This specific arrangement was chosen because it maximizes the uniform distribution of B-site cations, thereby avoiding artificial local clustering in a small supercell, and it represents the lowest energy state among several simple ordered models initially tested.

It should be noted that macroscopic $K(Ta_{0.5}Nb_{0.5})O_3$ is inherently a random solid solution. Ideally, true compositional disorder would be modeled using a large-scale Special Quasirandom Structure (SQS) containing hundreds of atoms. However, performing full geometric relaxations (including the *c*-axis) and highly converged Berry phase calculations with dense *k*-point sampling across a continuous ±30% strain

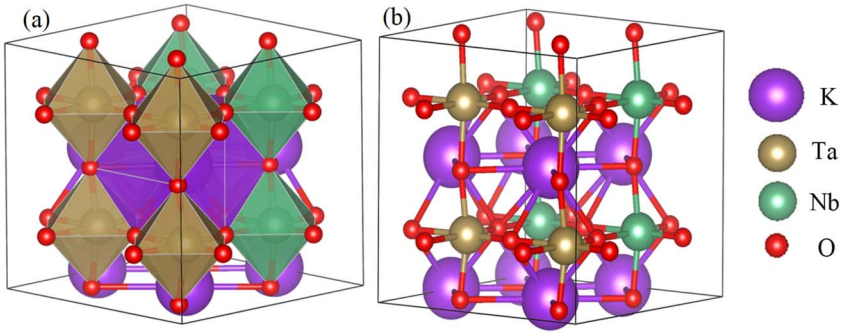

Fig. 1 KTN model diagram: (a) ball-and-stick; (b) polyhedral.

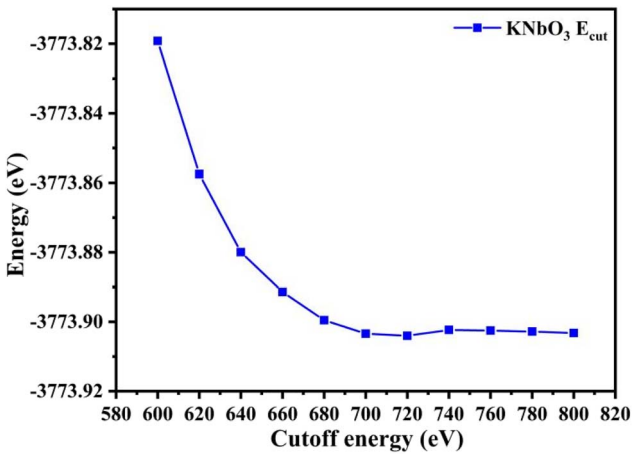

Fig. 2 Truncated energy convergence test diagram.

window for such a massive SQS supercell is currently computationally unfeasible. Therefore, the ordered 2 × 2 × 2 supercell is employed here as a representative local volume element to capture the intrinsic limits of the strain-induced physics, rather than a perfect statistical ensemble of the macroscopic alloy. While local configurational disorder may introduce subtle quantitative fluctuations, the qualitative physical trends regarding strain dependence remain highly robust.

Based on this representative model, biaxial strain ranging from −30% to 30% was applied to the KTN system in increments of 5%, with negative and positive values corresponding to compressive and tensile strains, respectively, while the *c*-axis remained fixed. All first-principles calculations based on density functional theory (DFT) were performed using the Vienna *Ab initio* Simulation Package (VASP).[19] The exchange-correlation energy was treated within the generalized gradient approximation (GGA) using the Perdew–Burke–Ernzerhof (PBE) functional.[20] A plane-wave cutoff energy of 720 eV was adopted, as determined from the convergence test conducted on the $KNbO_3$ system (Fig. 2). The Brillouin zone was sampled using a 3 × 3 × 3 *k*-point grid generated by the Monkhorst–Pack scheme,[21] and the electronic convergence criterion was set to 1.0×10^{-6} eV. The valence electron configurations considered in the calculations were as follows: K ($4s^1$), Nb ($4d^4\ 5s^1$), Ta ($5d^3\ 6s^2$), and O ($2s^2\ 2p^4$).

3 Analysis and discussion

3.1. Structural stability analysis

3.1.1. Structure. Table 1 summarizes the phase diagram of the KTN crystal structure under various biaxial strain conditions. As indicated, the system adopts a monoclinic phase under compressive strains ranging from −30% to −25%. When the compressive strain is reduced to between −20% and −15%, the structure transitions to an orthorhombic phase. Further decreasing the strain to −10% leads to a reversion to the monoclinic phase, while at −5% compressive strain, the system transforms again into the orthorhombic phase. These results demonstrate that as compressive strain is progressively reduced, the system undergoes two distinct phase transitions from monoclinic to orthorhombic symmetry.

To enhance the rigor of the physical property assessment of the intrinsic $K(Ta_{0.5}Nb_{0.5})O_3$ (KTN) system, we conducted *Ab Initio* Molecular Dynamics (AIMD) simulations. Fig. 3 presents a graph of the total energy of the intrinsic system varying with simulation time (fs). During the 8000 fs (8 ps) simulation, the total energy rapidly increased in the initial stage and then

Table 1 The crystal system of KTN under different strain effects

Strain/Pa	−30%	−25%	−20%	−15%	−10%	−5%	0	5%	10%	15%	20%	25%	30%
Crystal system	Monoclinic		Orthogonal		Monoclinic	Orthogonal	Tetragonal			Monoclinic			
Structural diagram													

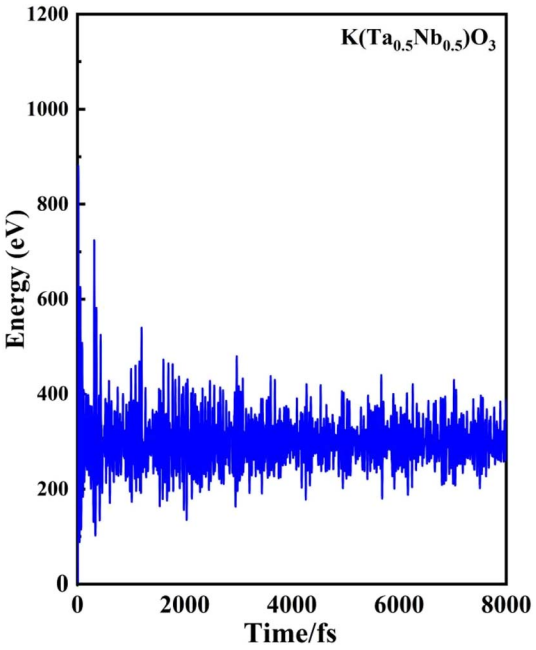

Fig. 3 *Ab Initio* molecular dynamics.

stabilized, oscillating within a fixed range. Notably, no significant energy drift was observed throughout the simulation time window, indicating that the system had reached and maintained a good thermodynamic equilibrium. This validates the reliability of the data extracted from this simulation, providing a benchmark for accurately calculating the band structure, density of states, and optical descriptors of the intrinsic system. Based on this reliable intrinsic benchmark, we will systematically analyze in the subsequent sections how the photocatalytic performance of KTN is modulated by strain engineering within the strain range of −30% to +30%.

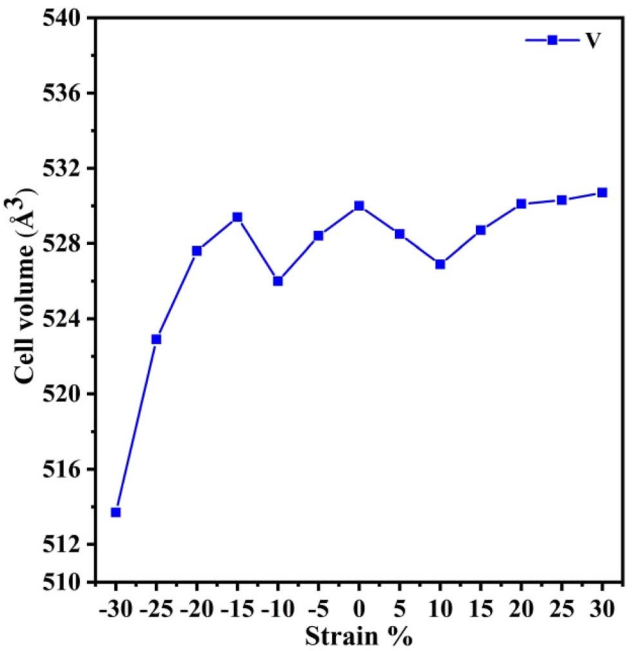

Fig. 4 The volume change of KTN systems under different strain effects.

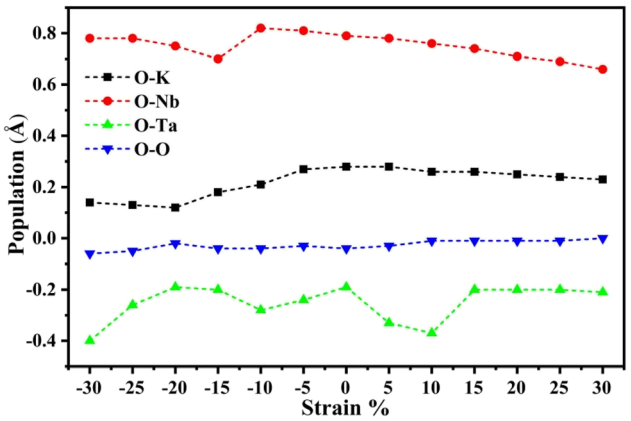

Fig. 5 Projected crystal orbital occupation numbers for key bonds in KTN under biaxial strain.

On the other hand, under tensile strains of 5% to 30%, the structure evolves from a tetragonal phase to a monoclinic phase, reflecting significant lattice distortion within the KTN system. With increasing tensile strain, the crystal structure shows a tendency toward stabilization, which aligns with previous findings reported by Noheda *et al.*[22] For visual illustration, Fig. 4 presents the variation in the volume of KTN as a function of biaxial strain. The volume trend is consistent with the phase transition behavior described above: external strain induces crystal distortion, resulting in corresponding volumetric changes.[23]

3.1.2. Projected crystal orbital occupation number. As illustrated in Fig. 5, the projected crystal orbital populations (rather than traditional Mulliken populations) of the KTN system under varying strain conditions reveal distinct trends for different bonds. With increasing strain, the O–K bond population initially decreases, then increases, before decreasing again, reaching its maximum values at 0% and 5% strain. A similar non-monotonic behavior is observed for the O–Nb bond, which also decreases, increases, and subsequently decreases, attaining a maximum at −10% strain. In contrast, the O–Ta bond exhibits fluctuating values, with minima occurring at −30% and 10% strain and maxima at −20% and 0% strain. The O–O bond population, meanwhile, changes relatively gradually and shows an overall increasing trend. It is noteworthy that the projected population magnitude serves as a direct indicator of covalent bond strength.[22]

As shown in Fig. 5, the projected populations of O–K and O–Nb bonds are positive under strain, indicating a dominant bonding character. In contrast, those of O–Ta and O–O bonds exhibit negative values. It is important to clarify that these negative populations do not imply unphysical negative electron densities; rather, they strictly reflect an anti-bonding character in these specific interactions, where the corresponding electronic states are spatially nodal between the atoms. Nevertheless, the net total population-defined as the sum of the

projected populations of O–K, O–Nb, O–Ta, and O–O interactions-remains positive across all strain conditions. This indicates that the bonding interactions dominate over the local anti-bonding states, ensuring that the overall global covalency and structural stability of the system are largely preserved. Among these, the O–Nb interaction exhibits the highest positive population, suggesting it provides the strongest covalent contribution. In summary, strain modulates the chemical bonds within the KTN system to varying degrees, with the O–Ta bond experiencing the most significant strain-induced variation. Importantly, the applied strain does not compromise the net global covalency, thereby offering a stable structural foundation for tuning and potentially enhancing the photocatalytic performance of the material.

In this study, the structural stability of the KTN system before and after strain application was further evaluated by calculating the binding energy, using the following formula:[24]

$$E_b = E_{\text{total}} - \frac{1}{N}(n_{\text{k}}E_{\text{k}} + n_{\text{Ta}}E_{\text{Ta}} + n_{\text{Nb}}E_{\text{Nb}} + n_{\text{O}}E_{\text{O}}) \quad (1)$$

In eqn (1), E_{total} denotes the total energy of the entire KTN crystal supercell. The symbols n_{k}, n_{Ta}, n_{Nb}, and n_{O} represent the number of potassium (K), tantalum (Ta), niobium (Nb), and oxygen (O) atoms in the calculated supercell model, respectively. E_{k}, E_{Ta}, E_{Nb}, and E_{O} refer to the energies of isolated free atoms of the corresponding elements. N is the normalization factor, typically defined as the number of formula units in the supercell. As shown in Fig. 6, the binding energy analysis indicates that under tensile strain (5% to 30%), the absolute binding energy of the system remains between −7.92 eV and −7.91 eV, closely matching that of the unstrained KTN system (−7.92 eV). This suggests that tensile strain has a limited effect on the structural stability. In contrast, under compressive strain (−30% to −5%), the absolute binding energy declines to between −7.3 eV and −7.9 eV, indicating that compressive lattice distortion slightly reduces structural stability. Notably, the binding energy remains negative across all strain conditions, confirming that each configured system is thermodynamically stable. This feature offers theoretical support for the practical application of KTN materials under various strain environments.

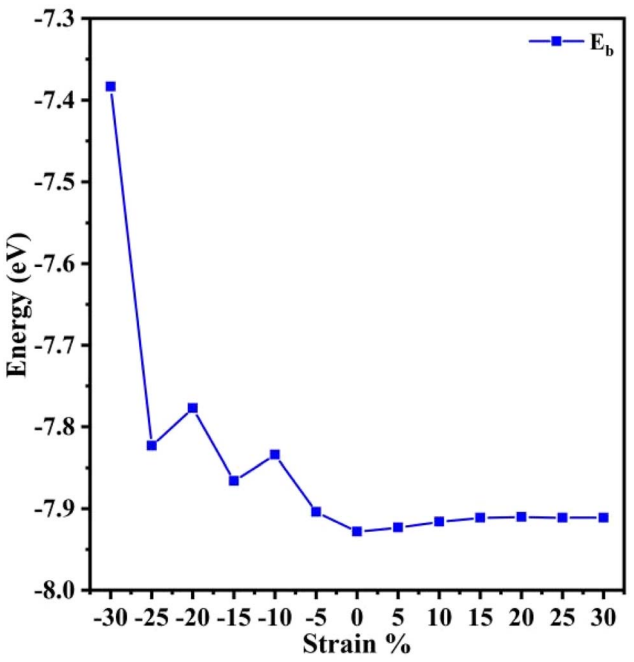

Fig. 6 The variation of binding energy in KTN systems under different strain effects.

3.1.3. Polarization intensity and effective mass. The core mechanism for enhancing the photocatalytic performance of the ferroelectric material KTN lies in its spontaneous polarization (P_{s}) and carrier migration characteristics. Primarily, P_{s} arises from the relative displacement of positive and negative charge centers within the unit cell, resulting in a directional electric dipole moment and an internal built-in electric field. This field plays a critical role in promoting the efficient separation of photogenerated electron–hole pairs. To rigorously quantify this effect and ensure the absolute physical validity of the computed polarization, our calculations were performed using the Berry phase method under stringent computational protocols. Specifically, to guarantee high accuracy in the integration, strict electronic parameters were adopted, including PREC = Accurate, an energy cutoff of 720 eV, an electronic convergence criterion of 1.0×10^{-6} eV, and a dense k-point mesh of $3 \times 3 \times 3$. At each biaxial strain point, the internal atomic coordinates and the c-axis were fully relaxed until residual forces were below 0.01 eV Å^{-1} prior to the electronic property calculations. Furthermore, an adiabatic path approach-interpolate intermediate structures between an ideal non-polar cubic perovskite reference (Pm3m) and the fully relaxed polarized state-was utilized to track the correct physical branch and explicitly avoid unphysical polarization quanta. Based on this highly robust computational framework,our results (Fig. 7(a)) clearly demonstrate that biaxial strain serves as an effective tool for modulating P_{s} Specifically, under the theoretical limit of 30% tensile strain, P_{s} is projected to reach 0.248 C m^{-2}, far exceeding its intrinsic value of 0.039 C m^{-2} (this result is consistent with the experimental value of 0.046 C m^{-2}).[25] Meanwhile, the extreme compressive strain can theoretically elevate P_{s} to 0.231 C m^{-2}. This strain-induced modulation of P_{s} is directly correlated with photocatalytic activity: a larger P_{s} corresponds to a stronger internal electric field, which more effectively suppresses carrier recombination. It is noteworthy that under all strain conditions, the P_{s} values of KTN remain higher than the intrinsic state (>0.039 C m^{-2}), underscoring the potential of strain engineering to continuously enhance photocatalytic quantum efficiency *via* the polarization field.[26]

Secondly, the effective mass serves as a key indicator for evaluating carrier mobility, offering critical insight into the migration behavior of electrons and holes within the system. It is therefore an essential parameter for assessing photocatalytic performance. In this study, we calculated the effective masses of electrons and holes in the KTN system both prior to and

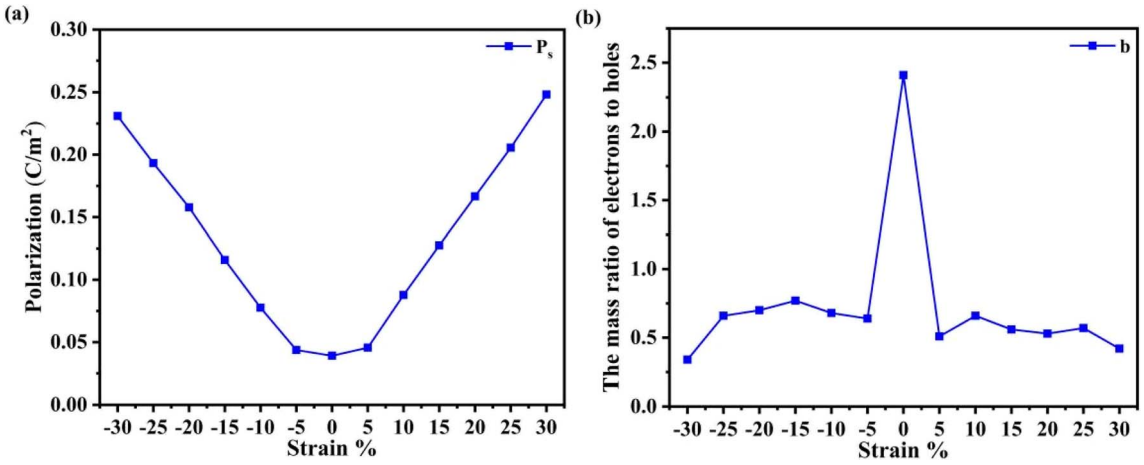

Fig. 7 (a) The variation of polarization intensity values of KTN system under different strain effects; (b) the ratio of the effective masses of electrons and holes in the KTN system before and after the application of strain.

following strain application. The effective mass is given by the following formula:[27]

$$m^* = \hbar^2 \Big/ \left(\frac{\partial^2 E}{\partial k^2}\right) \quad (2)$$

In this study, energy values are expressed in units of $1/(2\pi/a)^2$ eV, with $\hbar = h/2\pi$. Fig. 7(b) presents the calculated electron (m_e) and hole (m_h) effective masses in the KTN system before and after strain application. It should be emphasized that the reported effective masses are strictly anisotropic values rather than spatial averages. Specifically, they were derived through parabolic fitting of the conduction band minimum (CBM) and valence band maximum (VBM) along the Gamma $\rightarrow$ X direction, which corresponds to the in-plane [100] crystallographic axis. This specific direction was deliberately selected because the biaxial strain is applied exclusively within the *ab*-plane. The modulation of the in-plane lattice parameters directly dictates the orbital overlap within this plane, thereby governing the in-plane carrier mobility. For our photocatalytic system, optimizing this in-plane migration is of paramount importance. Previous studies have indicated that a significant difference between electron and hole effective masses leads to higher electron mobility within the system.[28] A key observation is that all strained configurations exhibit $m_h > m_e$, indicating that the material behaves as a "heavy-hole, light-electron" system. Since carrier mobility μ is inversely proportional to the effective mass ($\mu \propto 1/m$), the large disparity in effective masses-reflected by a small ratio $b = m_e/m_h^*$-implies that electron mobility is substantially higher than that of holes.[29] As a result, electrons migrate rapidly to the material surface, while holes migrate more slowly. As illustrated in Fig. 7(b), the b values for all strained systems are lower than that of the strain-free case. This pronounced asymmetry in effective masses promotes efficient spatial separation of photogenerated carriers, thereby suppressing recombination and significantly enhancing the photocatalytic activity of the material.

A broader mapping of various strain conditions reveals that the system subjected to −30% compressive strain exhibits the most pronounced synergistic optimization of these relevant physical parameters. This theoretical enhancement can be attributed to three primary factors: a reduced band gap, as confirmed by band structure analysis, which improves visible-light absorption and increases the concentration of photogenerated charge carriers; a significant effective mass difference between holes and electrons ($m_h >> m_e$), facilitating efficient electron migration and spatial charge separation; and a sustained polarization level (>0.039 C m^{-2}), which remains higher than that of the intrinsic state (0.023 C m^{-2}) and thereby supplies an internal electric field that further promotes charge separation.

Therefore, the application of compressive strain leads to a synergistic optimization of the band structure, carrier mobility, and polarization properties, pointing towards a remarkable enhancement in the photocatalytic performance

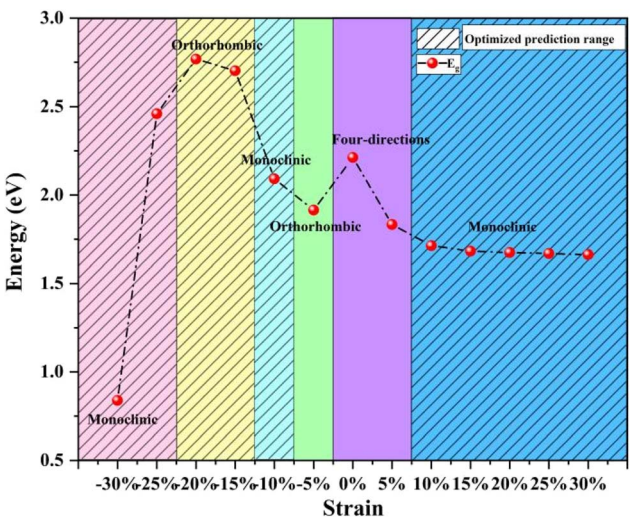

Fig. 8 Curve of band gap variation of KTN system under different stress conditions.

of KTN materials. While realizing strains as large as ±30% remains an experimental challenge-serving here primarily as a computational tool to map the intrinsic physical boundaries of the material-it is highly encouraging that the monotonic, favorable trends in bandgap reduction and polarization enhancement are already well-established within the currently accessible experimental window (*e.g.*, ±5%). These robust physical trends provide valuable insights and a feasible guiding strategy for designing high-performance ferroelectric photocatalysts.[30]

3.2. Electronic structure

3.2.1. Band structure. Fig. 8 displays the band diagrams of the KTN system under various strain conditions, illustrating that the system maintains a direct bandgap transition across all applied strains. To bridge our theoretical predictions with physical reality, particular attention was paid to the experimentally achievable strain window (±5%) *via* epitaxial growth, highlighted by the shaded area in Fig. 8. The results indicate that even within this realistic and feasible range, the bandgap of the material exhibits significant tunability. Specifically, compared to the intrinsic unstrained state, both +5% tensile strain and −5% compressive strain lead to a moderate reduction in the bandgap. This narrowing trend is highly favorable for photocatalytic applications, as it typically implies an enhanced capacity to absorb. a broader spectrum of solar light.

Beyond this practical experimental window, exploring a broader theoretical strain range reveals a more complex correlation between structural phase transitions and electronic properties. In general, tensile strain proves more advantageous than compressive strain for modulating the energy gap. Under tensile strain, the system undergoes a straightforward structural transition from a tetragonal to a monoclinic phase, and the energy gap gradually decreases as the strain increases (up to +30%), remaining consistently lower than that of the unstrained KTN. In contrast, under compression, the system experiences a more complex series of phase changes: initially from tetragonal to monoclinic, then to orthorhombic, and finally back to monoclinic. While a mild compression (down to −10%) continues to reduce the bandgap, a distinct threshold exists. When the compression is further enhanced to the range of −15% to −25%, the phase transition to the orthorhombic crystal system causes the energy gap to increase significantly compared to the original KTN. This increase limits the extension of its sunlight response range and impairs photocatalytic activity, an observation corroborated by subsequent optical property analyses. Further increasing the compressive strain to −30% causes the energy gap to drop sharply to 0.838 eV, eventually driving the system from a semiconducting to a metallic state, which is highly undesirable for photo catalysis.

These findings highlight that the photocatalytic performance of the KTN system is fundamentally tied to its structural phase. The monoclinic phase is particularly noteworthy, as it exhibits both structural stability and a reduced bandgap, providing optimal conditions for enhanced photocatalytic efficiency. Although the actual photocatalytic efficiency is governed by a complex interplay of various factors-such as carrier separation efficiency and band edge alignments-our results clearly demonstrate that appropriate strain manipulation is a powerful tool. Applying moderate strain, particularly within the experimentally accessible ±5% range, provides an effective and practical means to promote the excitation of electrons from the valence band to the conduction band, enhance carrier mobility, and ultimately optimize the material's potential photocatalytic activity without inducing structural degradation or phase instability.

3.2.2. Density of states diagram. Fig. 9(a) presents the projected density of states (PDOS) for each component in the KTN system. It can be observed that the valence band is predominantly contributed by the O-2p states, with minor contributions from Nb-4d and Ta-5d states. Notably, the O-2p states produce pronounced peaks within the energy ranges of −2 to −1 eV and −1 to 0 eV, indicating a high concentration of electrons in these regions. The conduction band, on the other

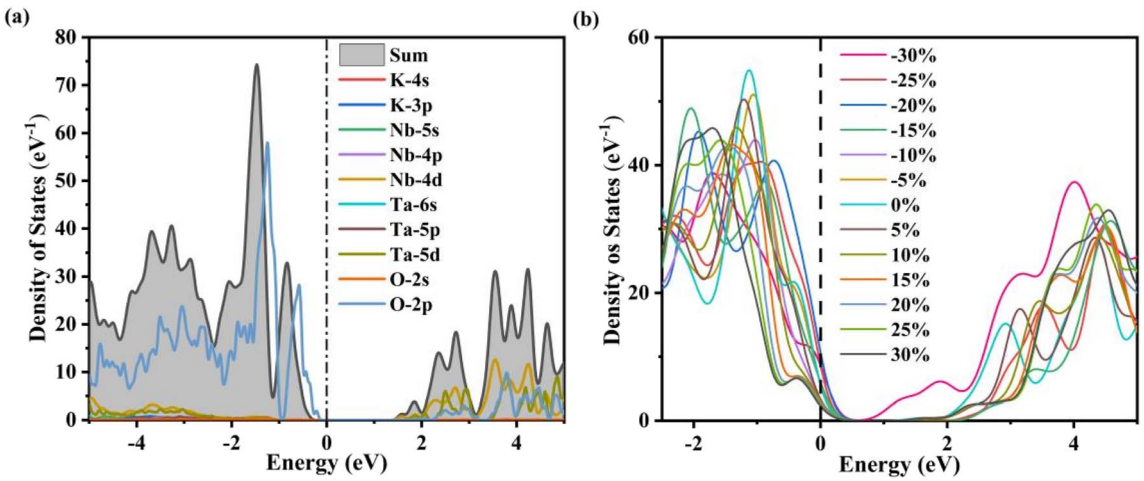

Fig. 9 (a) Shows the atomic state density diagram of each component in the KTN system; (b) shows the total state density diagram of the KTN system under different strain effects.

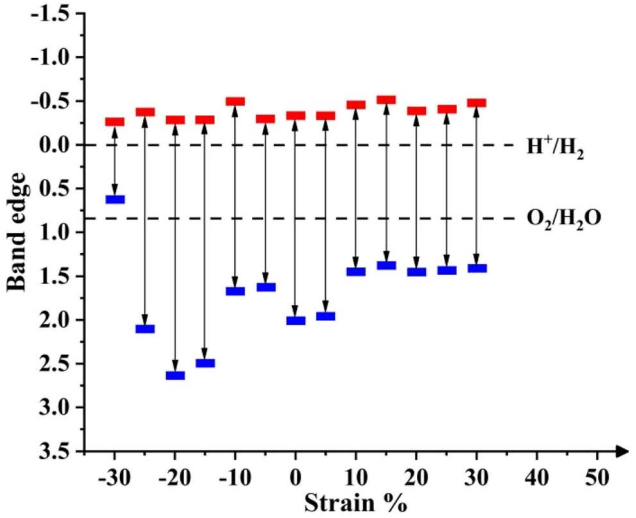

Fig. 10 Shows the edge positions of the water oxidation–reduction potential band of KTN under different strain effects.

hand, arises primarily from the hybridized interactions of O-2p, Nb-4d, and Ta-5d states, forming distinct hybridization peaks that facilitate electronic transitions. Compared to the conduction band, the valence band exhibits a broader distribution of electronic states. These findings are consistent with the typical electronic structure of perovskite materials, where the valence band is mainly composed of O-2p orbitals, while the conduction band is dominated by the outermost orbitals of B-site cations (Nb and Ta).[32]

As shown in Fig. 9(b), which displays the PDOS near the Fermi level under various strain conditions, all systems exhibit a tail effect in the valence band.[33] Specifically, under −20% compressive strain, the valence band shifts closer to the Fermi level, whereas under −30% compressive strain, the conduction band moves toward the Fermi level. This shift explains the reduction in the band gap of KTN under applied strain, which aligns well with the trends observed in the band structure analysis.

3.2.3. With borders included. Fig. 10 presents the band edge positions of the KTN system under various strain conditions, demonstrating that strain engineering significantly modulates the material's photocatalytic hydrogen evolution activity. Within the compressive strain range of −25% to −30%, the conduction band minimum (CBM) of all systems lies above the H^+/H_2 reduction potential, while the valence band maximum (VBM) remains below the O_2/H_2O oxidation potential, indicating that their band alignments thermodynamically satisfy the requirements for photocatalytic water splitting.

Notably, under −30% compressive strain, although the CBM remains higher than the H^+/H_2 potential-thus still enabling hydrogen evolution-its position decreases significantly, resulting in a diminished reduction driving force. Moreover, excessive compression may induce detrimental changes in the intrinsic material properties, ultimately impairing overall photocatalytic performance.

Comparative analysis reveals that tensile strain systems (particularly within 10% to 30%) generally exhibit stronger redox capabilities, as reflected by higher CBM and lower VBM positions. However, it is identified that both −5% compressive strain and 10–30% tensile strain constitute an optimal strain window. Within this range, the systems not only fulfill the thermodynamic criteria for both hydrogen and oxygen evolution reactions but also possess a moderate band gap-sufficiently narrow for enhanced light absorption yet wide enough to promote effective charge carrier separation.

Therefore, applying appropriate strain (*e.g.*, −5% compressive or 10–30% tensile) effectively optimizes the band structure of KTN, leading to enhanced redox capability for efficient water splitting and extended solar absorption range. These synergistic effects collectively contribute to the significantly improved photocatalytic activity of the system.[34]

3.3. Optical properties

3.3.1. Absorption spectrum. Fig. 11 displays the optical absorption edges of the KTN system under various strain conditions. As illustrated, the absorption edge of the system remains within the visible light range (1.6–3.9 eV) under both tensile and compressive strains. Compared to the unstrained KTN system, a red shift[31] is observed under −5% and −10% compressive strain as well as under 10–30% tensile strain; however, these systems exhibit weaker solar light absorption capability than pristine KTN.[35]

In contrast, under −30% compressive strain, the absorption edge shifts further toward the far-infrared region, which can be attributed to the significantly reduced band gap, resulting in the strongest solar absorption among all configurations. Additionally, systems subjected to compressive strains from −30% to −15% and tensile strain of 5% exhibit a broader range of solar light absorption compared to the unmodified KTN.

These findings demonstrate that applying appropriate strain can effectively enhance the photocatalytic performance of KTN by modulating its optical absorption characteristics.

3.3.2. Dielectric function. Fig. 12(a) displays the real part of the dielectric function. A larger static dielectric constant

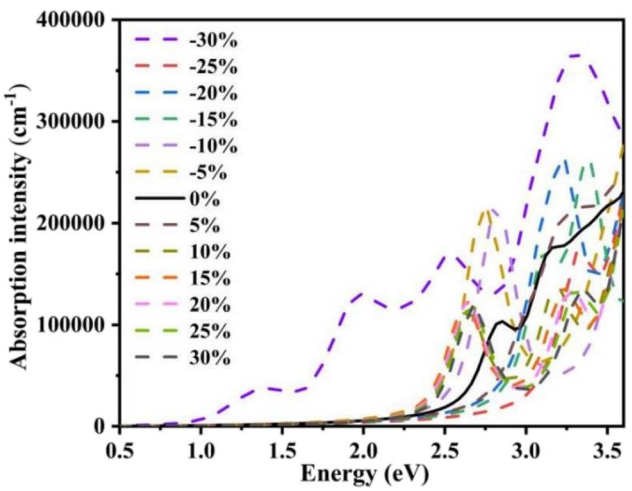

Fig. 11 Absorption of KTN system under different strain effects.

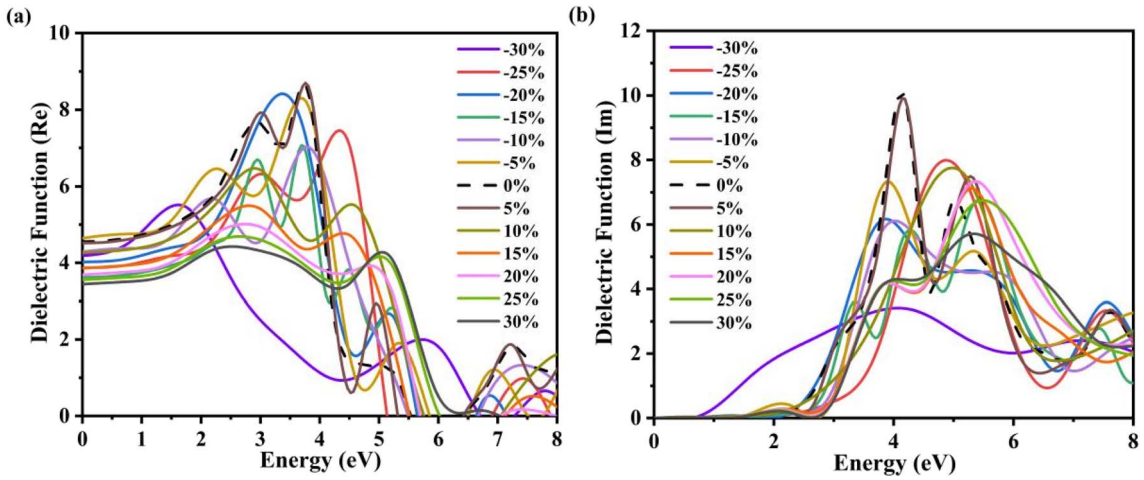

Fig. 12 Dielectric function diagrams of the KTN system under different strain effects: (a) real part of the dielectric function diagram; (b) imaginary part of the dielectric function diagram.

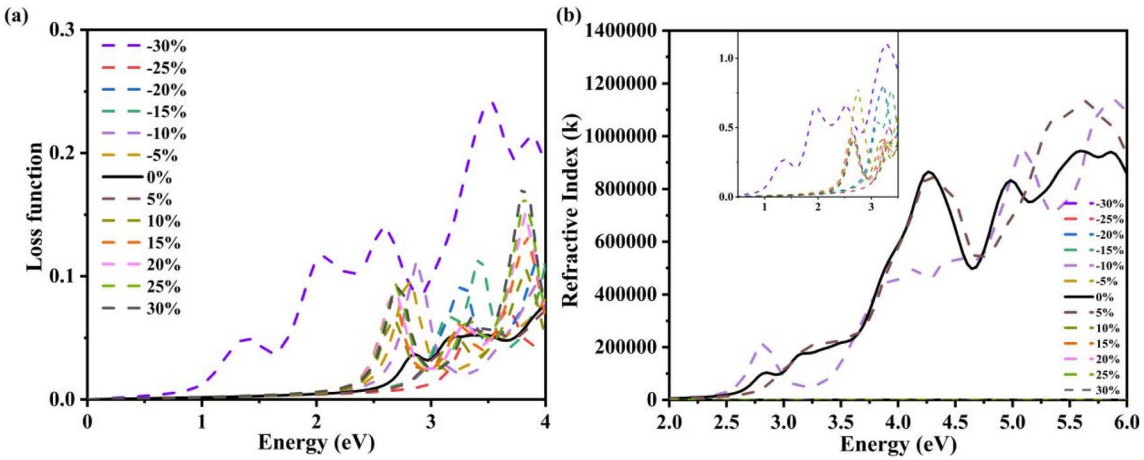

Fig. 13 Optical properties of KTN system under different strain effects: (a) energy loss diagram; (b) extinction coefficient diagram.

indicates a stronger capacity for charge binding and enhanced polarization capability within the system. Among all configurations, the system under −5% strain exhibits the highest static dielectric constant, corresponding to the most pronounced polarization behavior, which is beneficial for improving photocatalytic activity.

Fig. 12(b) presents the imaginary part of the dielectric function, where the first peak occurs at 3.8121 eV. The results indicate that applied strain enhances the polarization response of KTN to electrons and induces a red shift across various strain conditions. Furthermore, the sunlight response range is significantly broadened under strains ranging from −20% to −5% as well as at 30% tensile strain.

3.3.3. Energy loss and extinction coefficient. Fig. 13(a) presents the energy loss function of the KTN system, which represents the energy loss of electrons traversing the material. The observed peaks correspond to plasmon resonance. As shown in the figure, the peaks for systems under compressive strains from −30% to −10% and tensile strain of 5% all shift toward higher energy. Compared to the unstrained KTN, these systems exhibit increased energy loss values, indicating a rise in their plasmon resonance frequencies.

The extinction coefficient, another key optical property relevant to photocatalytic performance, is shown in Fig. 13(b). It can be observed that under compressive strains from −30% to −15% and tensile strain of 5%, the extinction coefficients are higher than that of the pristine KTN system. This suggests enhanced resistance to optical bleaching and improved photon absorption capability in these strained systems.

4 Conclusions

Based on first-principles calculations, this study systematically investigates the crystal structure, Mulliken population, polarization intensity, electronic structure, effective mass, band edge positions, and optical properties of KTN under biaxial strain ranging from −30% to 30%. The results demonstrate that the structural stability of KTN is preserved under all strain

conditions. A phase transition from tetragonal to monoclinic symmetry is observed with increasing strain, with tensile-strained systems exhibiting superior structural stability compared to compressively strained ones.

Mulliken population analysis confirms enhanced covalent character across the strained systems, consistent with the high overall bond populations. The polarization intensity increases significantly with strain, promoting efficient separation of photogenerated electron–hole pairs and thereby improving photocatalytic efficiency.

Compressive strain induces a continuous reduction in band gap, reaching a minimum of 0.838 eV at −30% strain, which substantially facilitates electron transitions. The system consistently exhibits a "heavy-hole, light-electron" character ($m_h^*/m_e^* \approx 2.4$), enhancing carrier mobility and enabling both charge carriers to surpass redox potentials. A pronounced redshift in the absorption edge under specific strains-particularly between −30% to −15% compression and 5% tension-extends the visible-light response range.

Notably, at −30% compressive strain, KTN stabilizes in the monoclinic phase and achieves optimal performance in polarization, carrier mobility, and light absorption, leading to the highest photocatalytic activity. These findings highlight strain-engineered KTN as a highly promising ferroelectric photocatalyst for efficient solar hydrogen production. This work offers valuable theoretical guidance for the design of strain-modulated KTN-based photocatalytic materials.

It should be emphasized that the intrinsic properties investigated in this paper, such as spontaneous polarization, carrier effective mass, and band edge alignment, are essentially thermodynamic and kinetic descriptors of the photocatalytic potential of the material. Although these descriptors define the material's ability to absorb light, the initial charge separation, and the theoretical driving force for water splitting, they cannot be directly equated with the actual photocatalytic hydrogen production rate. The actual catalytic performance ultimately depends on complex surface phenomena beyond the scope of bulk analysis, including surface terminations, the Gibbs free energy of intermediate adsorbed states (ΔG_{H^*}), interfacial band bending, defect chemistry, and detailed reaction barrier kinetics. Therefore, the optimal strain state determined here represents the most favorable internal conditions and can serve as a fundamental blueprint for subsequent surface-level research.

Author contributions

Conceptualization, X. W., L. L. Z.; methodology, X. W., L. L. Z.; investigation, X. W., L. L. Z.; software, X. W., L. L. Z.; writing – original draft, X. W., L. L. Z., R. X., Y. M. Z., Q. Y. C., C. Z., X. Y. Z., and H. M. Y.; writing – review and editing, N. Y. N., L. L. Z., and X. W.; funding acquisition and project administration, H. M. Y., and L. L. Z.

Conflicts of interest

The authors declare that they have no competing interests and there are no conflicts.

Data availability

The data that support the findings of this study are available from the corresponding authors upon reasonable request.

Supplementary information (SI) is available. See DOI: https://doi.org/10.1039/d5ra09223j.

Acknowledgements

This work is financially supported by Xinjiang Natural Science Foundation (Grant No. 2024D01C48), the Science and Technology Plan Project of Yili State the Special Project (Grant No. YZ2022B021).

References

1 Q. Zhu, K. Zhang, D. Li, *et al*, Polarization-enhanced photocatalytic activity in non-centrosymmetric materials based photo catalysis: A review, *Chem. Eng. J.*, 2021, **426**, 131681.
2 T. Abe, S. Kim, C. Moriyoshi, *et al*, Visualization of spontaneous electronic polarization in Pb ion of ferroelectric $PbTiO_3$ by synchrotron-radiation x-ray diffraction, *Appl. Phys. Lett.*, 2020, **117**, 252905.
3 J. Ji, Y. Pu, L. Chang, *et al*, Boosting the separation of bulk charge in $Na_{0.5}Bi_{0.5}TiO_3$ by the synergetic effect of ferroelectric polarization and thin-sheet shape, *Ceram. Int.*, 2021, **47**, 27650–27659.
4 X. Huang, R. Lei, J. Yuan, *et al*, Insight into the piezo-photo coupling effect of $PbTiO_3$/CdS composites for piezo-photocatalytic hydrogen production, *Appl. Catal., B*, 2021, **282**, 119586.
5 X. Liu, B. Lv, Z. Ding, *et al*, External uniaxial compressive strain induced built-in electric field in bilayer two-dimensional As_2S_3 for photocatalytic water splitting: A first-principles study, *Appl. Surf. Sci.*, 2021, **535**, 147701.
6 L. Zhu, D. Liu, X. Shi, *et al*, Ultrahigh piezoelectric performances of (K, Na) NbO_3 based ceramics enabled by structural flexibility and grain orientation, *Nat. Commun.*, 2025, **16**, 901.
7 C. Manspeaker, G. Merrion, K. Krouse, *et al*, Ambient processing conditions and their effects on perovskite device performance, *Cryst. Res. Technol.*, 2022, **57**, 2100116.
8 C. Xu, P. Hang, C. Kan, *et al*, Molecular ferroelectric self-assembled interlayer for efficient perovskite solar cells, *Nat. Commun.*, 2025, **16**, 835.
9 S. Kuk, K. Ko, B. H. Kim, *et al*, Channel Mobility and Inversion Carrier Density in MFIS FEFET: Deep Insights Into Device Physics for Non-Volatile Memory Applications, *IEEE J. Electron Devices Soc.*, 2024, **13**, 8–14.
10 X. Xu, G. Lai, K. Su, *et al*, First-principles study on the elastic, electronic and photocatalytic properties of multiferroic material $InFeO_3$ under strain, *Int. J. Mod. Phys. B*, 2021, **35**, 2150215.
11 X. Liu, J. Wang, F. Ling, *et al*, Mechanical control of photo catalysis in 2D ferroelectrics, *Sol. RRL*, 2023, **7**, 2300589.

12 Z. He, W. Li, J. Yang, *et al*, Tuning ferroelectric photovoltaic performance in R3c-$CuNbO_3$ through compressive strain engineering: a first-principles study, *RSC Adv.*, 2023, **13**, 34475–34481.
13 D. Lu, D. J. Baek, S. S. Hong, *et al*, Synthesis of freestanding single-crystal perovskite films and heterostructures by etching of sacrificial water-soluble layers, *Nat. Mater.*, 2016, **15**, 1255–1260.
14 H. Zhang, J. Tersoff, S. Xu, *et al*, Approaching the ideal elastic strain limit in silicon nanowires, *Sci. Adv.*, 2016, **2**, e1501382.
15 J. Suntivich, K. J. May, H. A. Gasteiger, *et al*, A perovskite oxide optimized for oxygen evolution catalysis from molecular orbital principles, *Science*, 2011, **334**, 1383–1385.
16 H. Mao, B. Chen, J. Chen, *et al*, Recent advances in high-pressure science and technology, *Matter Radiat. Extremes*, 2016, **1**, 59–75.
17 C. Porwal, G. Singh, M. Sharma, *et al*, Progress and Outlook of Ferroelectric/non-Ferroelectric Polar Glass-Ceramics for Multi-Catalytic Applications, *Prog. Solid State Chem.*, 2024, **77**, 100497.
18 D. Takhar, B. Birajdar and R. K. Ghosh, Photocatalytic and piezocatalytic properties of h-NbP and h-NbN monolayers for green hydrogen production: Insight from density functional theory calculations, *J. Phys. Chem. C*, 2023, **127**, 3408–3416.
19 H. Okadome Valencia, B. Wang, G. Frapper, *et al*, New developments in the GDIS simulation package: Integration of VASP and USPEX, *J. Comput. Chem.*, 2021, **42**, 1602–1626.
20 M. S. Zahan, M. R. Munshi, M. Z. Rana, *et al*, Theoretical insights on geometrical, mechanical, electronic, thermodynamic and photocatalytic characteristics of $RaTiO_3$ compound: a DFT investigation, *Comput. Condens. Matter*, 2023, **36**, e00832.
21 J. U. Rehman, M. A. Rehman, M. Usman, *et al*, First-principles calculations to investigate structural, electronics, optical and mechanical properties of $LaRu_2P_2$ compound for superconducting application, *Mol. Simul.*, 2023, **49**, 76–84.
22 Y. Gao, Q. Zhang, W. Hu, *et al*, First-principles computational screening of two-dimensional polar materials for photocatalytic water splitting, *ACS Nano*, 2024, **18**, 19381–19390.
23 A. Kumer, K. A. Hoque, U. Chakma, *et al*, First-principles investigations on the conducting photocatalytic behaviour in $SrZr_xGe_{1-x}O_3$ ($x = 1$, 0.96, 0.92 and 0.88), *Sci. Rep.*, 2025, **15**, 9336.
24 A. Raturi, P. Mittal and S. Choudhary, Electronic and optical properties of lithium niobate ($LiNbO_3$) under tensile and compressive strain for optoelectronic applications: Insights from DFT-computations, *Mater. Sci. Semicond. Process.*, 2022, **144**, 106606.
25 Y. Zhang, S. Li, F. Liu, *et al*, Growth and characterization of large size lead-free ferroelectric K (Ta, Nb) O_3 single crystal, *J. Am. Ceram. Soc.*, 2021, **104**, 5182–5191.
26 F. Liu, X. Zhuang, Z. Du, *et al*, Enhanced photocatalytic performance by polarizing ferroelectric $KNbO_3$ for degradation of plastic wastes under mild conditions, *Appl. Catal., B*, 2022, **318**, 121897.
27 S. Wang, L. Su, Y. Qiu, *et al*, Enhanced thermoelectric performance in Cl-doped $BiSbSe_3$ with optimal carrier concentration and effective mass, *J. Mater. Sci. Technol.*, 2021, **70**, 67–72.
28 G. Wang, J. Zhang, C. Huang, *et al*, First-principles study of structural, elastic, electronic, transport properties, and dielectric breakdown of Cs_2Te photocathode, *Sci. Rep.*, 2025, **15**, 2780.
29 J. Zhang, W. Yu, J. Liu, *et al*, Illustration of high-active Ag_2CrO_4 photocatalyst from the first-principle calculation of electronic structures and carrier effective mass, *Appl. Surf. Sci.*, 2015, **358**, 457–462.
30 J. Liu, L. Yin and G. Liu, Ferro/Nonferroelectric Vertical Heterostructure Superlattice as a Visible-Light-Responsive Photocatalyst: A DFT Prediction, *ACS Appl. Mater. Interfaces*, 2024, **16**, 7026–7037.
31 J. Wen, Z. Luo, L. Fang, *et al*, Photoinduced ferroelectric phase transition triggering photocatalytic water splitting, *npj Comput. Mater.*, 2025, **11**, 112.
32 X. Lu, Z. Zhao, K. Li, *et al*, First-principles insight into the photoelectronic properties of Ge-based perovskites, *RSC Adv.*, 2016, **6**, 86976–86981.
33 T. Li, S. Deng, H. Liu, *et al*, Insights into strain engineering: from ferroelectrics to related functional materials and beyond, *Chem. Rev.*, 2024, **124**, 7045–7105.
34 Y. Miao, Y. Zhao, S. Zhang, *et al*, Strain engineering: a boosting strategy for photo catalysis, *Adv. Mater.*, 2022, **34**, 2200868.
35 J. Ren, J. Zhang, B. Tian, *et al*, First-principles study of the electronic, optical adsorption, and photocatalytic water-splitting properties of a strain-tuned SiC/WS_2 heterojunction, *Int. J. Hydrogen Energy*, 2024, **87**, 554–565.